Journal of Materials Chemistry A

Accepted Manuscript

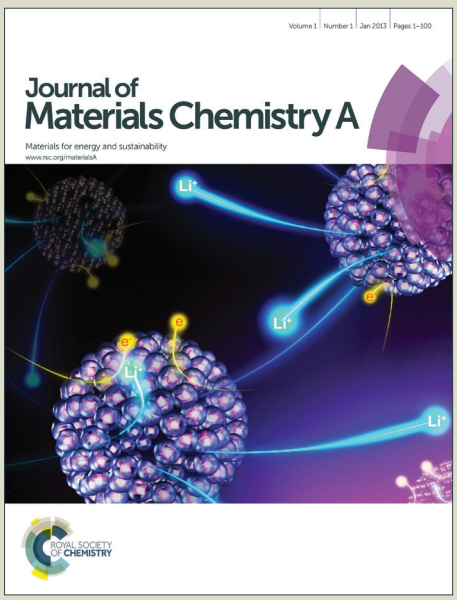

ROYAL SOCIETY OF CHEMISTRY

www.rsc.org/materialsA

Table of Contents

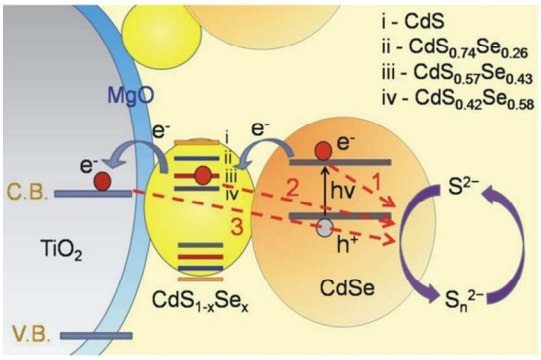

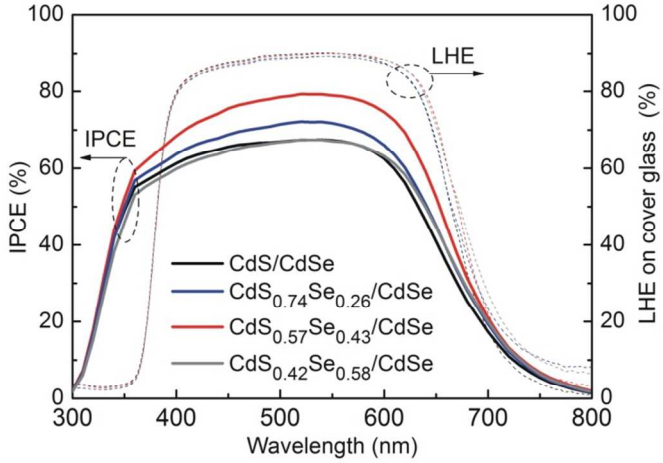

A facile way to enhance electron injection efficiency of solar cells by interlayer $CdS_{1-x}Se_x$ quantum dots has been developed.

Journal of
Materials Chemistry A

RSCPublishing

ARTICLE

Band Alignment by Ternary Crystalline Potential-Tuning Interlayer for Efficient Electron Injection in Quantum Dot-Sensitized Solar Cells

Cite this: DOI: 10.1039/x0xx00000x

Zhenhua Chen[a], Wenqin Peng[a], Kun Zhang[a], Jing Zhang[a], Xudong Yang*[a], Youhei Numata[a], and Liyuan Han*[a,b]

Received 00th January 2012,
Accepted 00th January 2012

DOI: 10.1039/x0xx00000x

www.rsc.org/

We developed a facile way to enhance electron injection efficiency in CdSe based quantum dot–sensitized solar cells (QDSCs) by introducing a potential-tuning interlayer composed of ternary $CdS_{1-x}Se_x$ quantum dots (QDs) between TiO_2 film and CdSe QDs. A suitable band structure for electron injection was obtained when the composition of Se was 0.43 in the $CdS_{1-x}Se_x$ interlayer. The $TiO_2/CdS_{0.57}Se_{0.43}$/CdSe QDSCs achieved a photocurrent density 17.8% higher than conventional TiO_2/CdS/CdSe QDSCs. The enhanced performance is owing to the tuned energetic driving force simultaneously adequate for both exciton dissociation at $CdS_{1-x}Se_x$/CdSe interface and electron injection at $TiO_2/CdS_{1-x}Se_x$ interface. The electron injection also benefited probably from reducing the lattice mismatch between TiO_2 film and CdSe QDs by inserting crystalline $CdS_{1-x}Se_x$ interlayer. Our findings indicate that introducing of a ternary crystalline potential-tuning interlayer with specifically designed band alignment is a promising strategy to enable efficient electron injection in QDSCs.

1. Introduction

QDs sensitized solar cells (QDSCs) have been widely investigated in past few years. Compared with traditional dyes, semiconductor QDs (QDs) possess high molar extinction coefficient[1,2] and size tunable optical absorptions,[3] making them a promising candidate as novel light harvesters. Moreover, QDs may open up new ways to utilize hot electrons[4] or generate multiple charge carriers with a single photon,[5,6] to break up the Shockley-Queisser limit (32%) and improve efficiencies. However, the power conversion efficiency reported for QDSCs are still much lower than the dye sensitized solar cells (>10%), which attributes to the relatively low electron injection rate and high charge recombination in QDSCs.[7,8]

To improve the performance of QDSCs, introducing an interlayer between the metal oxide electrode and quantum dot sensitizers has been developed in recent years. For example, semiconducting CdS was used as an interlayer to form a TiO_2/CdS/CdSe photoanode. By changing the growth cycle/crystal size of the interlayer, the band structure was tuned and the energy conversion efficiency of the cell was improved.[9] Similar method were reported in ZnO/CdS/CdSe and TiO_2/PbS/CdS photoanodes, in which the band structures of QDs were modified and the electron injection was expected to be maximized with reduced recombination.[10, 11] In addition, interlayers with matched lattice parameters could increase the loading quality of QDs and enhance the optical absorption;[12] while some interlayers having favorable band structures benefited the electrons injection from QDs to TiO_2 nanoparticles.[13,14] Herein the band alignments by the introduced interlayer, especially at the new generated interfaces on its both sides, are crucial to the electron injection efficiency, charge recombination, and the performance of QDSCs. However, there is rare study to demonstrate how the band alignments at both interfaces of the interlayer affect the performance of QDSCs.

Using ternary crystalline potential-tuning interlayer is an efficient way to optimal band alignments and has been successfully applied in many optoelectronic devices, such as light emitting diode (LEDs)[15,16] and laser diode (LDs)[17,18], but it is still rarely reported in QDSCs. By modulating the constituent stoichiometries of ternary QDs interlayer, the potential of conduction band can be changed more easily than that of binary QDs interlayer, and so that the band offset at both interfaces can be finely adjusted. In addition, homogenous ternary QDs may have less defects than doped QDs in which more trap states could increase the non-radioactive recombination and demonstrate a relatively low FF (<50%).[19-21] Therefore, homogenous ternary QDs are promising candidate for potential-tuning interlayer to improve QDSCs performance.

In this work, we employed a surface ion transfer method to synthesize ternary alloy $CdS_{1-x}Se_x$ ($0<x<1$) QDs as an interlayer in CdSe QDs sensitized solar cells. We controllably changed the band offset at the interfaces of $TiO_2/CdS_{1-x}Se_x$ and $CdS_{1-x}Se_x$/CdSe by modulating the constituent stoichiometries of the $CdS_{1-x}Se_x$ QDs interlayer, so that the electrons injection was tuned. Besides, the $TiO_2/CdS_{1-x}Se_x$ and $CdS_{1-x}Se_x$/CdSe interfaces possessed less lattice mismatch than TiO_2/CdSe interface, which facilitated the deposition of CdSe QDs and electron injection. Compared with conventional binary CdS QDs interlayer, the developed $CdS_{0.57}Se_{0.43}$ QDs interlayer enabled 15% higher electron injection efficiency and 17.8% larger photocurrent density, and the carrier lifetime was also

increased by 58% in corresponding QDSCs. The improved performance was attributed to the tuned energetic driving force simultaneously adequate for both the exciton dissociation at the $CdS_{1-x}Se_x$/CdSe interface and the electron injection at the TiO_2/$CdS_{1-x}Se_x$ interface. Hence the introducing of a ternary crystalline potential-tuning interlayer is a promising way for band alignment to achieve efficient electron injection in QDSCs.

2. Experimental section

2.1 TiO_2 mesoporous film preparation and treatment.

Highly crystalline TiO_2 paste was synthesized by hydrolysis of titanium isopropoxide in ethanol via a sol–gel route.[22] The porosity of the paste was controlled by the addition of various amounts of ethyl cellulose. A dense, transparent film (~6 µm in thickness) of TiO_2 nanoparticles (20 nm in diameter) and a scattering layer (~5 µm thick, 400-nm-diameter nanoparticles) were screen-printed onto fluorine-doped tin oxide glass in that order. The substrate was sintered at 500 °C for 1 h to generate anatase nanocrystals. After sintering, the TiO_2 electrode was immersed in 40 mM aqueous $TiCl_4$ at 70°C for 30 min. The film was then annealed at 450°C for 30 min. In the following step, the TiO_2 photoanode was dipped into ethanol containing 0.02 M magnesium acetate for 2 min and annealed at 450°C for another 30 min to form an ultrathin MgO layer on the TiO_2 surfaces.

2.2 Preparation of double-layer $CdS_{1-x}Se_x$/CdSe QDs

The TiO_2 electrodes were first treated by dipping drops of thioglycolic acid, allowed to stand for 1 min, and completely dried in a nitrogen flow. The electrodes were immersed in ethanol containing $Cd(NO_3)_2{\cdot}4H_2O$ (0.1 M) and then in methanol containing $Na_2S{\cdot}5H_2O$ (0.1 M). Following each immersion, the electrodes were rinsed for 30 s to remove excess precursor. This dipping cycle was repeated three more times to deposit the binary CdS QDs onto the TiO_2 films. The interfacial ternary $CdS_{1-x}Se_x$ QDs were obtained by surface selenization of the CdS QD–decorated TiO_2 substrate. A Se^{2-} source solution was prepared by dissolving Se (2.5 mM) in a solution of $NaBH_4$ (5 mM) in distilled water. Ion transfer between Se and S was performed on CdS QD surfaces at 50°C under Ar, with reaction times of 1, 10, and 30 min. The samples were then washed with distilled water and dried in a nitrogen flow. We annealed the samples at 230°C for 15 min under Ar to convert the gradient $CdS_{1-x}Se_x$ QDs into homogeneous ternary alloys. The outer layer CdSe QDs were deposited by immersion of the electrode into ethanol containing $Cd(NO_3)_2{\cdot}4H_2O$ (0.03 M) and transparent oxygen-free Se^{2-} (0.03 M) solution, respectively. Seven cycles of CdSe QD deposition were performed.

2.3 Characterization of nanocrystals.

Morphology and phase structure were determined with a scanning electron microscope (JSM-6500F, JEOL) and a transmission electron microscope (JEM-2100F, JEOL). The atomic ratio of each element in the interlayer $CdS_{1-x}Se_x$ QDs were obtained by Energy-dispersive X-ray (EDX) spectroscopy, which is integrated in a scanning electron microscope (SEM). The semiconductor QDs were examined by X-ray photoelectron spectroscopy (XPS, PHI Quantera SXM, Japan) using Al K_α radiation. Absorption spectra were recorded with a Lambda-750 UV/Vis spectrophotometer (Perkin Elmer). LHE measurement was carried out on a thin cover glass (0.14 mm). TiO_2 was deposited onto the cover glass plate and covered with a drop of an aqueous solution and another thin glass plate. The aqueous solution was used because water is used as the electrolyte solvent in QDSCs. The transmittance and absorbance spectra of bare and QD-sensitized TiO_2 films were measured by means of the integrating sphere detector in the spectrophotometer. LHE was obtained by adding the absorbed photon ratios on the front side and the back side. Photoelectron spectroscopy (AC-3, Riken) was used to determine the ionization potentials of the semiconductor QDs; the analysis was performed under a 0.2 L/min N_2 flow.

2.4 Solar cell assembly and performance.

The TiO_2 photoanodes decorated with $CdS_{1-x}Se_x$/CdSe QDs were coated with a thin ZnS layer before device construction, to passivate the charge carrier traps induced by dangling orbitals and surface defects. The ZnS coating was applied by dipping the QD-decorated TiO_2 substrates alternately into $Zn(NO_3)_2$ (0.1 M) and Na_2S (0.1 M) aqueous solutions. The dipping procedure was repeated once. For the counter electrode, we employed a fluorine-doped tin oxide glass coated with a thin film of Cu_2S, which was prepared by a chemical bath deposition process. The reaction was conducted at 70°C for 1 h with a mixture of 25 mM $Cu(SO_4)_2{\cdot}5H_2O$ and 25 mM $Na_2S_2O_3{\cdot}5H_2O$ in an oxygen-free aqueous solution. The photovoltaic cells were assembled by hot pressuring the TiO_2/$CdS_{1-x}Se_x$ electrode, a Cu_2S-coated counter electrode, and a 25-µm-thick sealing spacer (Surlyn, Solaronix). We used a polysulfide electrolyte with a S^{2-}/S_x^{2-} redox pair, which was prepared with the following composition: Na_2S (1 M), S (1 M), and NaOH (0.1 M).

The $J-V$ characteristics of the solar cells were measured by using a black metal mask with an aperture area of 0.2304 cm^2 under standard air mass 1.5 sunlight (100 mW/cm^2, WXS-90S-L2, Wacom Denso Co., Japan). The scan mode was conducted from short circuit to open circuit. IPCE values were measured with monochromatic incident light (10^{16} photon/cm^2) under 100 mW/cm^2 white bias light in DC mode (CEP-2000, Bunko-Keiki).[23]

2.5 Analysis of solar cell devices.

IMPS and IMVS were carried out with a frequency response analyzer (Solartron-1255B) and a potentiostat/galvanostat (Solartron-SI1287) combined with a laser source (excitation wavelength, 446 nm). The light intensity was varied using a controller (DPS3002, Neoark). The electrochemical impedance spectra were obtained on an electrochemical workstation (Solartron 1287 and 1255B) with a two-electrode system under 1 sun illumination. For the open-circuit voltage decay study, the cell was illuminated until V_{oc} was stable. The illumination was turned off with a shutter. The open-circuit voltage decay was recorded with an Ecochemie potentiostat equipped with a short-interval sampling module. The decay analysis refers only to values measured after closing of the shutter for full darkness.

3. Results and discussion

Ternary $CdS_{1-x}Se_x$ ($0<x<1$) QDs, in which Cd, S, and Se atoms were homogenously distributed, were grown on MgO-coated TiO_2 film. The strategy for synthesis of ternary $CdS_{1-x}Se_x$ QDs is based on a surface ion exchange method.[24,25] The solubility product constant (K_{sp}) of CdSe (1.4×10^{-35}) is much smaller (8 orders of magnitude)

than that of CdS (8×10^{-27}). This implies that the CdS QDs can be used as sacrificial templates to synthesize more stable CdSe by an anion exchange process. Firstly, the CdS QDs were in-situ decorated onto MgO-coated TiO_2 using a SILAR method. After surface selenization of the CdS QDs with Se^{2-} ions in aqueous solution, some of the S^{2-} ions were replaced by Se^{2-} from the surface to center of the QDs; this process was controlled by adjusting the ion exchange time and temperature. The Se concentration decreases from the surface to center in these $CdS_{1-x}Se_x$ QDs, while the concentration of S increases correspondingly. The anions would start to cross the crystal grain boundary of the QDs after annealing at 230°C in an Ar atmosphere, producing the homogeneous alloy structure for ternary $CdS_{1-x}Se_x$ QDs ($0 \le x \le 1$).

Herein, the purpose of involving the thin MgO layer was to reduce the number of surface traps and defective states on TiO_2 nanocrystals. An atomic model of a ternary $CdS_{1-x}Se_x$ QD, in which the Cd, S, and Se atoms are homogenously distributed, is shown in Fig. 1a. CdSe QDs were deposited as a light-absorption layer by means of the SILAR process, in seven cycles; these conditions were previously shown to provide co-sensitized QDSCs with the best performance.[26] The photoanode structure is illustrated in Fig. 1b. In this structure, the interlayer $CdS_{1-x}Se_x$ QDs play two important roles. First, the energy band of the ternary nanocrystals can be tuned by changing the Se content. The CBM of annealed $CdS_{1-x}Se_x$ nanocrystals is shifted downward relative to the CBM of CdS buffer layers, to produce a staircase band alignment with CdSe QDs; and this shift facilitates charge injection from the QDs into the TiO_2 nanoparticles. Second, the lattice mismatch between $CdS_{1-x}Se_x$ and CdSe is less than 4%,[24] which promotes deposition of CdSe QDs and enhances light harvesting at long wavelengths.

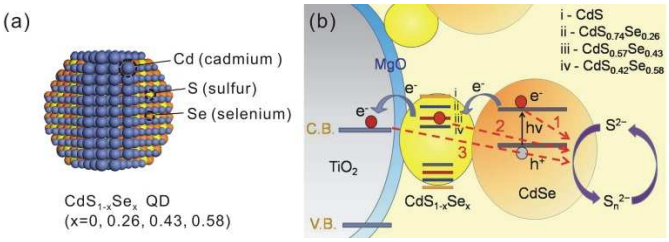

Fig. 1 (a) Atomic model of a ternary $CdS_{1-x}Se_x$ QD. (b) Schematic illustration of interfacial charge transfer and recombination in $CdS_{1-x}Se_x$/CdSe QDSCs.

There are three main pathways for recombination between excited electrons in different semiconductor nanocrystal layers and holes in the polysulfide electrolyte (Fig. 1b, red arrows). The presence of interlayer $CdS_{1-x}Se_x$ QDs with favorable band energy is the key to maximizing electron injection and reducing charge recombination. An overhigh interlayer CBM will introduce a potential barrier at the $CdS_{1-x}Se_x$/CdSe interface, blocking charge transfer and increasing recombination between electrons in the CdSe QDs and holes in the electrolyte (recombination 1). In contrast, an extremely low interlayer CBM will not drive electrons toward TiO_2 and will thus increase the probability of recombination (recombination 2).

The morphology of TiO_2 nanoparticles decorated with $CdS_{1-x}Se_x$/CdSe QDs was examined by high-resolution transmission electron microscopy (HRTEM, Fig. 2a–c). The fringe spacing of 0.35 nm matched the interplanar distance of the (100) planes in cubic anatase TiO_2 (Fig. 2a). Fig. 2b reveals a decorated $CdS_{1-x}Se_x$ (x = 0.43) QD with diameter ~5 nm. In the HRTEM image obtained after CdSe QD deposition (Fig. 2c), another layer of CdSe QDs with obviously different lattice fringes can be observed. These HRTEM results confirm that the QDs adsorbed controllably onto the TiO_2 nanoparticles are bi-layer structure.

The elemental compositions of representative $CdS_{0.57}Se_{0.43}$ QDs and the double-layer $CdS_{0.57}Se_{0.43}$/CdSe QDs were determined by X-ray photoelectron spectroscopy. The appearance of $Cd3d_{5/2}$ at 412.5 eV and $Cd3d_{5/2}$ at 405.3 eV (Fig. 2d); S2p at 163 eV and Se3p at 160.7 eV (Fig. 2e); and Se3d at 55 eV (Fig. 2e) in $CdS_{0.57}Se_{0.43}$ QDs confirmed the coexistence of Cd, Se, and S (black lines). After deposition of the CdSe QDs, the electrons originating from S atoms in the $CdS_{0.57}Se_{0.43}$ QDs were quenched by the outer layer CdSe QDs, so the probability of penetration of these electrons was low. Coincident with this quenching, the S2p peak of the $CdS_{1-x}Se_x$/CdSe QDs (red curve in Fig. 2e) disappeared (black curve in Fig. 2e). These results confirm that the $CdS_{1-x}Se_x$/CdSe QDs absorbed on the TiO_2 nanoparticle surfaces in a double-layer structure.

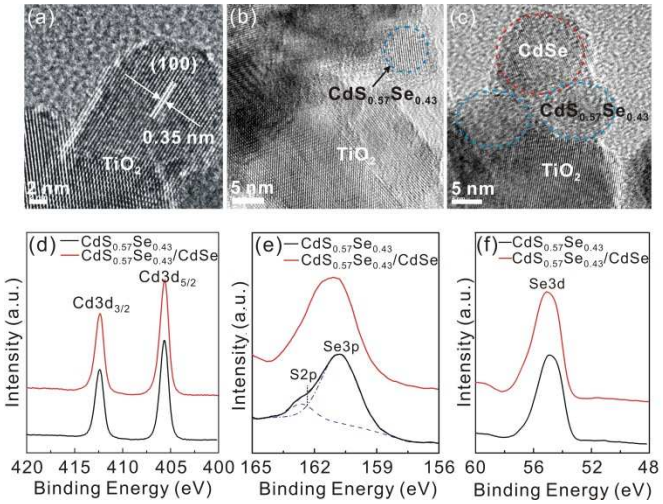

Fig. 2 High-resolution transmission electron micrographs of (a) bare TiO_2 nanoparticles, (b) TiO_2 nanoparticle film decorated with a $CdS_{1-x}Se_x$ QD (x = 0.43), and (c) photoanode further coated with a CdSe QD. X-ray photoelectron spectra (B.E., Binding Energy) of interfacial $CdS_{0.57}Se_{0.43}$ QDs and $CdS_{0.57}Se_{0.43}$/CdSe QDs: (d) Cd3d, (e) S2p and Se3p, and (f) Se3d.

To determine the band structure at the TiO_2/$CdS_{1-x}Se_x$/CdSe interfaces, we first evaluated the bandgap of the QDs layer-by-layer. We characterized ~6-μm-thick transparent film of TiO_2 nanoparticles (20 nm in diameter) sensitized with CdS QDs or with $CdS_{1-x}Se_x$ QDs of three different compositions (x = 0.26, 0.43 and 0.58). Energy-dispersive X-ray spectroscopy confirmed the atomic ratio of each element in the QDs (Fig. S1a). The optical absorption of the interlayer $CdS_{1-x}Se_x$ QDs was measured before and after CdSe QD deposition by means of UV–vis absorption spectroscopy. The characteristic absorption region in the spectrum of the CdS QDs was between 350 and 450 nm, which was attributed to the bandgap of these QDs. The absorption spectral range of the $CdS_{1-x}Se_x$ QDs was broadened relative to that of the CdS QDs. A red shift of the

absorbance band-edge was achieved in the spectral range of 490–600 nm by controlled incorporation of Se into the CdS QDs. The absorption edge after deposition of the outer layer CdSe QDs was further red shifted to 675 nm, which made the spectrum broad enough that the outer layer could act as the light-harvesting layer. Interestingly, after seven cycles of CdSe QD deposition on various $TiO_2/CdS_{1-x}Se_x$ photoanodes, the tail of the optical absorption spectrum became coherent. We estimated the optical bandgaps of the

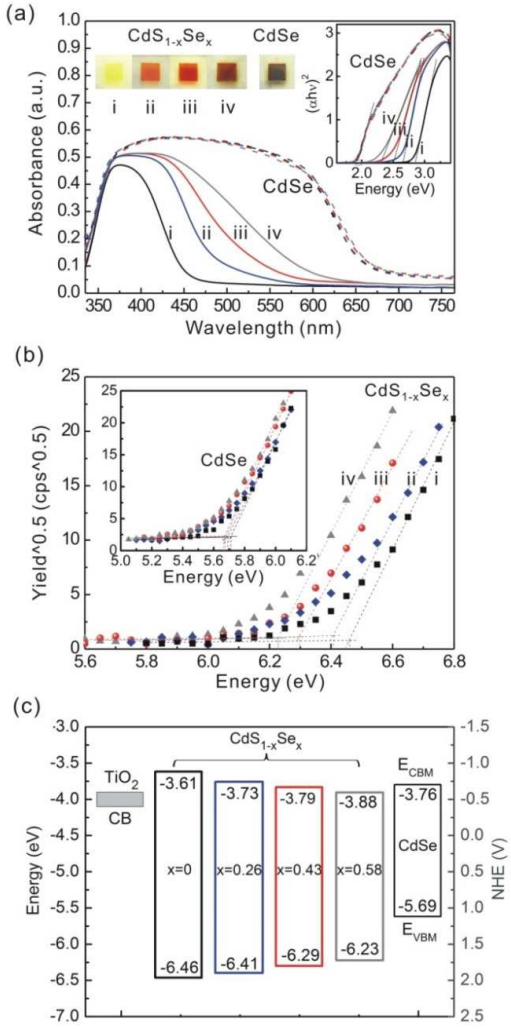

Fig. 3 (a) Absorbance spectra of four $CdS_{1-x}Se_x$ QDs measured on transparent TiO_2 films: (i) pristine CdS QDs and (ii–iv) $CdS_{1-x}Se_x$ QDs with Se fractions of 0.26, 0.43, and 0.58; left inset, images of the four $CdS_{1-x}Se_x$ QDs and a representative $CdS_{1-x}Se_x$/CdSe QD (x = 0.43); right inset, plots of $(\alpha h\nu)^2$ versus energy for $CdS_{1-x}Se_x$ samples. (b) Ionization spectra of (i) CdS QDs, (ii) $CdS_{0.74}Se_{0.26}$ QD, (iii) $CdS_{0.57}Se_{0.43}$ QD, and (iv) $CdS_{0.42}Se_{0.58}$ QD. The inset shows the spectra of the four QD samples further coated with CdSe QDs. (c) Band diagram at the $TiO_2/CdS_{1-x}Se_x$/CdSe interfaces; VBM, valence band maximum.

$CdS_{1-x}Se_x$ QDs and CdSe QDs by applying Tauc's law for direct bandgap semiconductors, plotting $(\alpha h\nu)^2$ against the photon energy (inset of Fig. 3a), where α is the absorption coefficient, and $h\nu$ is the photon energy.[27] For pristine CdS QDs and $CdS_{1-x}Se_x$ QDs with Se ratios of 0.26, 0.43, and 0.58, the optical bandgaps were determined to be 2.85, 2.68, 2.5, and 2.35 eV, respectively. After deposition of the CdSe QDs, the bandgap was 1.93 ± 0.02 eV.

Next we analyzed the QD ionization potentials, which correspond to their valence band maxima, by means of photoelectron spectroscopy (Fig. 3b). The bottom spectrum in Fig. 3b was obtained from pristine CdS QDs. The secondary electron cutoffs for the $CdS_{1-x}Se_x$ QDs were shifted toward lower ionization potential relative to the cutoffs for the CdS QDs. The positions of the valence band maxima with respect to the vacuum levels of pristine CdS, $CdS_{0.74}Se_{0.26}$, $CdS_{0.57}Se_{0.43}$, and $CdS_{0.42}Se_{0.58}$ QDs were –6.46, –6.41, –6.29, and –6.23 eV, respectively.

We had determined the bandgaps for the QDs based on Tauc's plots (inset in Fig. 3a), so we could obtain the positions of the CBM with respect to the vacuum levels obtained by adding both the valence band maxima and the bandgaps. The obtained CBM were –3.61, –3.73, –3.79, and –3.88 eV versus vacuum levels for interlayer CdS, $CdS_{0.74}Se_{0.26}$, $CdS_{0.57}Se_{0.43}$, and $CdS_{0.42}Se_{0.58}$ QDs. Employing the same approach, we determined the CBM of the QD samples to be 3.76 ± 0.02 eV after seven cycles of CdSe QD deposition.

As reported elsewhere, the VBM of TiO_2 is –7.5 eV with respect to vacuum level.[13,28] We investigated the absorbance and reflectance spectrum of MgO passivated TiO_2 nanoparticles, both of which confirmed its bandgap value is 3.5eV (Fig. S2). We can determine the CBM of surface treated TiO_2 nanoparticles, which is -4.0 eV versus vacuum levels, agreed with some reported values. [29]

The band diagram for the $TiO_2/CdS_{1-x}Se_x$/CdSe interfaces is illustrated in Fig. 3b. Herein, the conduction band potential of CdSSe locates lower than those of CdSe QDs, which is attributed to their size increases during annealing process. The CdS and $CdS_{0.74}Se_{0.26}$ nanocrystals generated type I nanoheterojunctions with CdSe QDs, whereas the $CdS_{0.57}Se_{0.43}$/CdSe and $CdS_{0.42}Se_{0.58}$/CdSe generated type II nanoheterojunctions at the TiO_2 nanoparticle surfaces.

Herein, our TiO_2/CdS/CdSe structure demonstrated a type I band alignment, which is contrary to some reported CdS/CdSe co-sensitized photoanodes.[13,30-32] This is due to the CdS QDs buffer layer we use is quite thin with small diameter, resulting in a large bandgap and high CBM value. This type I TiO_2/CdS/CdSe structure is in accordance with another report.[33]

It is noticed that the band energy of CdSe QDs on $CdS_{1-x}Se_x$ QDs interlayer and on TiO_2 is different due to the Fermi level alignment. The CBM of CdSe QDs on interlayer is –3.76 eV, while it is –3.91 eV on TiO_2. The CdSe QDs are shifted up, which is agree with the previously report.[13] As well, the band energy of interlayer $CdS_{1-x}Se_x$ may be shift down by outlayer CdSe deposition due to Fermi level pinning. From Fig. 3b, the shift of CdSe conduction band energy is 0.09 eV in different interlayer $CdS_{1-x}Se_x$ (x=0.43 and 0.58), while their interlayer CBM shifting is lower than 0.02 eV. Therefore, the band energy of annealed FTO/TiO_2/$CdS_{1-x}Se_x$ photoanode has slight effect by outlayer CdSe QDs, we did not count the down shift value.

A mesoporous TiO_2 nanoparticle film, consisting of a ~6-µm-thick, dense, transparent layer and a ~5-µm-thick scattering layer, was sensitized by $CdS_{1-x}Se_x$/CdSe QDs and used as the photoanode in QDSCs. Fig. S3a shows scanning electron micrographs of bare TiO_2 nanoparticles (upper part) and TiO_2 nanoparticles decorated with $CdS_{0.57}Se_{0.43}$/CdSe QDs (lower part). Tian et al. reported that the porosity of TiO_2 nanoparticles affects the performance of

QDSCs.[34] Therefore, we determined the pore size of the nanoparticles before and after coverage with the QDs. The transparent TiO_2 nanoparticles we prepared had an average diameter of 25 nm with a pore size of 25.0 ± 4 nm, as determined by the Brunauer–Emmett–Teller method. After coverage with the $CdS_{0.57}Se_{0.43}$/CdSe QDs, the surface of the TiO_2 nanoparticles was rough and the pore size became smaller. The double-layer $CdS_{0.57}Se_{0.43}$/CdSe QDs were effectively loaded onto the TiO_2 film, as demonstrated in the cross-sectional scanning electron micrograph shown in Fig. S3b. Cross-sectional mapping of Cd, S, and Se indicates that these elements were uniformly distributed throughout the photoanode.

Photocurrent density–voltage (*J-V*) curves of CdS/CdSe QDs and $CdS_{1-x}Se_x$/CdSe QDs were measured under 1 sun illumination (100mW/cm^2) in the presence of a S^{2-}/S_x^{2-} redox couple and a Cu_2S counter electrode. The interlayer $CdS_{1-x}Se_x$ QDs with a lower conduction band resulted in easier electron injection from the CdSe QDs to the TiO_2 nanoparticles. Consequently, larger short-circuit current density (J_{sc}) values were obtained for cells sensitized with $CdS_{1-x}Se_x$/CdSe QDs than for cells sensitized with CdS/CdSe QDs (Fig. 4a). Cells sensitized with the $CdS_{0.74}Se_{0.26}$/CdSe, $CdS_{0.57}Se_{0.43}$/CdSe, and $CdS_{0.42}Se_{0.58}$/CdSe QDs exhibited J_{sc} values of 13.42, 14.22, and 12.66 mA/cm^2, which were 1.35, 2.15, and 0.59 mA/cm^2 higher than the value obtained with the CdS/CdSe QDs (12.07 mA/cm^2). The performance characteristics obtained with the four types of QDs are summarized in Table 1. Note that the J_{sc} value obtained with $CdS_{0.42}Se_{0.58}$ QDs as the interlayer was 1.57 mA/cm^2 less than that obtained with the $CdS_{0.57}Se_{0.43}$ QDs, which have a lower Se content. The reason is that the difference between the CBM of the $CdS_{0.42}Se_{0.58}$ QDs and the TiO_2 nanoparticles (0.12 eV, Fig. 3c) was so close that the driving force for electron passing through the TiO_2/QD interfaces was not large enough. This result is in agreement with our explanation of charge recombination (Fig. 1b).

Compared with bare CdSe QDs (7 cycles) decorated TiO_2 nanoparticles, the improvement of J_{sc} in $TiO_2/CdS_{0.57}Se_{0.43}$/CdSe and $TiO_2/CdS_{0.42}Se_{0.58}$/CdSe based QDSCs can be contributed to the formation of type II heterojunction, which benefit the electron injection from CdSe QDs to TiO_2 photoanode. Besides, the interlayer $CdS_{1-x}Se_x$ has matched lattice parameters with CdSe, which could increase the loading quality of CdSe QDs and enhance the optical absorption, increasing the J_{sc}.

Table 1 Calculated J_{sc}, V_{oc}, FF, and η values for CdS/CdSe, $CdS_{1-x}Se_x$/CdSe and CdSe QDSCs under 1-sun illumination (100 mW/cm^2).

	J_{sc} (mA/cm^2)	V_{oc} (mV)	FF (%)	η (%)
CdS/CdSe	12.07	552.9	61.3	4.09
$CdS_{0.74}Se_{0.26}$/CdSe	13.41	546.5	57.5	4.22
$CdS_{0.57}Se_{0.43}$/CdSe	14.22	566.8	55.3	4.46
$CdS_{0.42}Se_{0.58}$/CdSe	12.65	569.3	49.7	4.14
CdSe	9.53	579.1	54.4	3.00

The monochromatic incident photon-to-electron conversion efficiency (IPCE) spectra confirmed the superiority of $CdS_{1-x}Se_x$/CdSe QDs as sensitizers (Fig. 4b). In principle, the IPCE of QDSCs depends on the LHE of the QDs, the efficiency of charge injection (Φ_{inj}) from the QDs into the TiO_2 nanocrystals, and the efficiency of charge collection by the glass-supported electrode (η_{coll}):[35]

$$IPCE = LHE \times \phi_{inj} \times \eta_{coll} \qquad (1)$$

The IPCEs of the four QDSCs showed obvious differences in the visible range but identical tails at 710 nm. The identical tails imply that the different J_{sc} values of the double-layer QDs should be attributed not to differences in light absorption but rather to differences in charge injection efficiency.

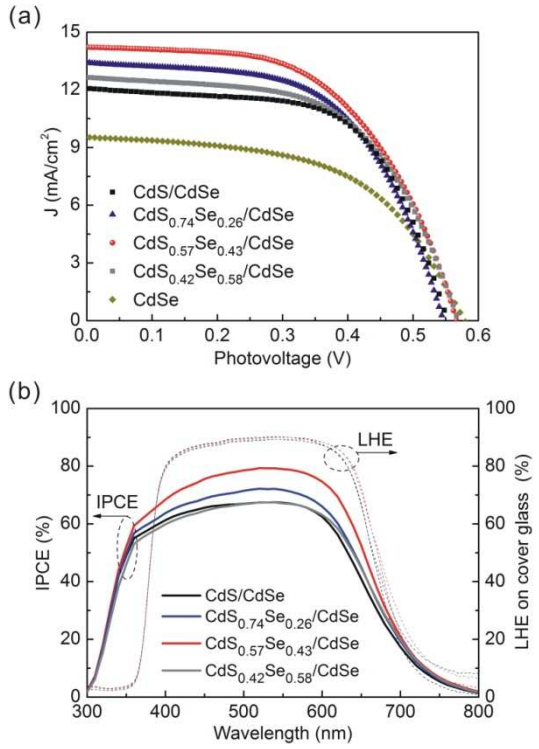

Fig. 4 (a) *J–V* characteristics of solar cells sensitized with CdS/CdSe QDs and $CdS_{1-x}Se_x$/CdSe QDs (x = 0.26, 0.43, and 0.58). (b) IPCE of the QD-sensitized solar cells. The LHEs of the corresponding QDs were measured on a thin cover glass.

We determined the LHEs of the CdS/CdSe QDs and three types of $CdS_{1-x}Se_x$ QDs/CdSe QDs (x = 0.26, 0.43, and 0.58) on a thin cover glass (0.14 mm) to avoid scattered light leaks from the glass substrate side (see the experimental section). Both transmittance (R%) and absorbance (T%) of bare and QDs sensitized TiO_2 films were measured by the integrating sphere detector. The LHE of QDs can be obtained from the difference in the spectra between the sensitized and unsensitized films (equation 2). ”

$$A_1\% = 1 - R_1\% (TiO_2) - T_1\% (TiO_2)$$
$$A_2\% = 1 - R_2\% (TiO_2/QDs) - T_2\% (TiO_2/QDs)$$
$$LHE = A_2\% - A_1\% \qquad (2)$$

The transmittance and reflectance spectra of bare TiO_2 film are shown in Fig. S4a. The light collection obtained by adding the

transmittance and reflectance spectra approached 100% above 400 nm. Fig. S4b shows the LHE of QD-sensitized films; light harvesting below 400 nm was assigned to absorption by the TiO_2 film.

We knew the LHEs of the QDs from the difference in absorptivity (%) between the sensitized and unsensitized films as determined with an integrating sphere detector. The band edge of the LHE spectra in Fig. 4b was kept at 710 nm for the different double-layer QDs. The LHEs of the QDs approached 90% at 550 nm owing to the high extinction coefficient of semiconductor QDs, the concentration of QDs, and the thickness of the absorbing layer we used. The nearly identical LHE spectra for the different $CdS_{1-x}Se_x$ QDs/CdSe QDs confirm that the differences in the IPCE spectra could not be attributed to the optical absorptions of the QDs.

Improving the charge collection efficiency of QDSCs requires optimization of both electron transport time (τ_{sc}) and electron recombination lifetime (τ_{oc}), which can be evaluated by intensity-modulated photocurrent spectroscopy (IMPS) and intensity-modulated photovoltage spectroscopy (IMVS). Typical IMPS and IMVS plots for representative solar cells based on $CdS_{1-x}Se_x$/CdSe (x = 0.43) QDs are shown in Fig. S5a, b. The τ_{sc} values can be calculated as $\tau_{sc} = 1/\omega_{min,sc} = 1/2\pi f_{min,sc}$, where $f_{min,sc}$ is the frequency of the lowest imaginary number in the IMPS plot.[36] The τ_{oc} values can be calculated as $\tau_{oc} = 1/\omega_{min,oc} = 1/2\pi f_{min,oc}$, where $f_{min,oc}$ is the frequency of the lowest imaginary number in the IMVS plot.[37] The calculated τ_{sc} and τ_{oc} values are presented in Table S1 for laser intensities from 20 to 50 W/m^2 (λ = 446 nm).

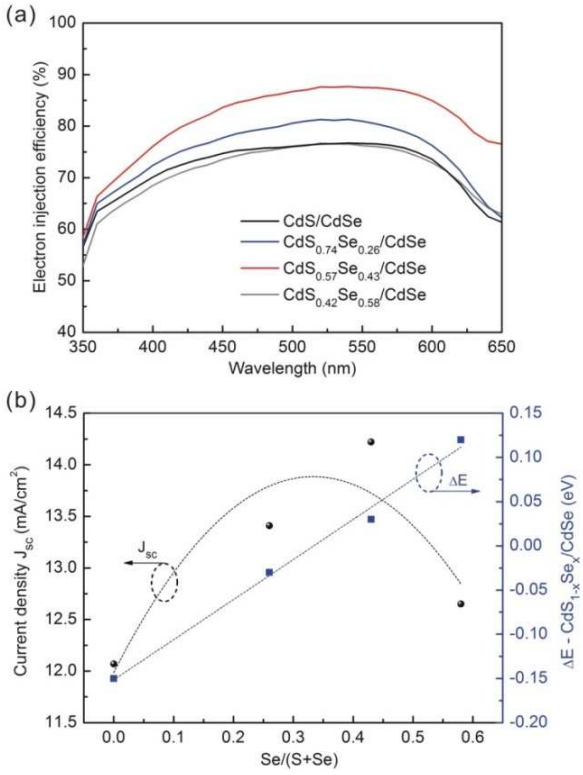

Fig. 5 (a) Plots of injection efficiency versus wavelength calculated for CdS/CdSe and $CdS_{1-x}Se_x$/CdSe QDSCs (x = 0.26, 0.43, 0.58). (b) Plots of J_{sc} and potential difference of $CdS_{1-x}Se_x$/CdSe heterojunctions versus Se content in the $CdS_{1-x}Se_x$ QD layer (x = 0, 0.26, 0.43, and 0.58).

Knowing the values of τ_{sc} and τ_{oc} allows us to calculate the collection efficiency of photogenerated electrons: $\eta_{coll} = 1/(1+ \tau_{sc}/\tau_{oc})$. Because τ_{oc} was generally at least ~9 times τ_{sc}, η_{coll} values of >90% were achieved. The calculated η_{coll} values for $CdS_{0.57}Se_{0.43}$/CdSe QDSCs and CdS/CdSe QDSCs under various illumination levels are shown in Table S1. The calculated η_{coll} values did not change markedly with light intensity, because the electron transport time and recombination lifetime have the same dependence on light intensity. The η_{coll} of the QDSCs was estimated at laser intensity (46.6 W/m^2) because the recorded V_{oc} at this intensity was close to that obtained at 1 sun illumination.

The dependence of electronic injection efficiency on wavelength was determined by dividing the IPCE by both the LHEs of QD-sensitized films (Fig. S4b) and the η_{coll} values (eq 1). The wavelength dependences of the electronic injection efficiencies of photoanodes sensitized with $CdS_{1-x}Se_x$/CdSe QDs and CdS/CdSe QDs are given in Fig. 5a. The staircase $CdS_{1-x}Se_x$/CdSe QDs enhanced the electron injection efficiency of the QDSCs; specifically, QDSCs with $CdS_{0.57}Se_{0.43}$ QDs as the interlayer showed 15% higher charge injection efficiency than that observed with CdS QDs. As a result, the photocurrent of $CdS_{0.57}Se_{0.43}$/CdSe-based QDSCs was substantially improved.

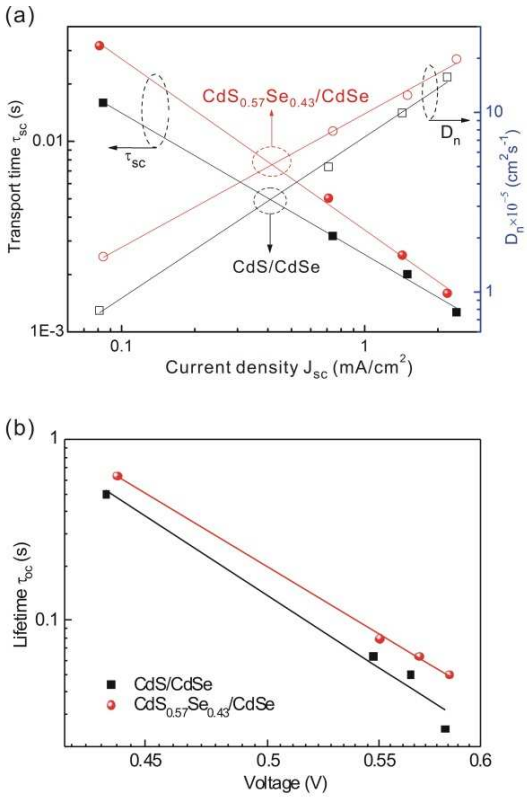

Fig. 6 (a) Dependence of electron transport time and diffusion coefficient on J_{sc} in CdS/CdSe and $CdS_{0.57}Se_{0.43}$/CdSe QDSCs, as measured by IMPS. (b) Dependence of electron lifetime on V_{oc} in CdS/CdSe and $CdS_{0.57}Se_{0.43}$/CdSe QDSCs, as measured by IMVS.

We also evaluated the dependence of J_{sc} and the CBM potential difference of $CdS_{1-x}Se_x$/CdSe heterojunctions on Se content, Se/(S + Se), in the ternary QDs. The CBM potential difference between

$CdS_{1-x}Se_x$ and CdSe QDs depended linearly on Se content, whereas J_{sc} was highest when $CdS_{0.57}Se_{0.43}$ QDs were used as the interlayer, and then decreased as the Se content was increased further. The photocurrent density depended on the electron injection efficiency, which is determined by the band alignment of the CBM of the two layers of semiconductor QDs and TiO_2. When the Se fraction was increased to 0.58, the difference between the CBM of $CdS_{1-x}Se_x$ and TiO_2 was <0.2 eV. This small potential difference could not sufficiently drive electrons toward TiO_2, and thus the charge injection efficiency and the J_{sc} were reduced.

To demonstrate the advantage of our developed $CdS_{1-x}Se_x$/CdSe QDSCs, we compared the charge transport and recombination in a representative TiO_2/$CdS_{0.57}Se_{0.43}$/CdSe photoanode with that in a typical TiO_2/CdS/CdSe photoanode (Fig. 6a). The logarithm of τ_{sc} was linearly related to J_{sc}, and electron transport in a TiO_2 film decorated with $CdS_{1-x}Se_x$/CdSe QDs was obviously faster than that in CdS/CdSe QDs in the low J_{sc} region (low laser intensity, ~20 W/m^2), whereas the difference was small in the high J_{sc} range (large laser intensity, ~50 W/m^2). The value of τ_{sc} is known to be affected by the thickness and the presence of electron traps distributed in the bandgap of nanocrystalline TiO_2. During the formation of the interlayer $CdS_{1-x}Se_x$ nanocrystals on the MgO-passivated TiO_2 surfaces, the annealing process may improve the crystallinity of the ternary QDs and reduce the number of surface states at the TiO_2/QDs interfaces, decreasing the charge transfer time. At higher illumination, the surface traps on the TiO_2 nanocrystals would be filled up by dense injected electrons, so the charge transport time would not be markedly affected by such trap states, and thus the difference in electron transfer time would be reduced. The electron diffusion coefficient (D_n) in TiO_2 can be calculated by the expression $D_n = d^2/\tau_{sc}$, where d is film thickness. Plots of D_n as a function of J_{sc} showed the same trend as plots of τ_{sc} (Fig. 6a).

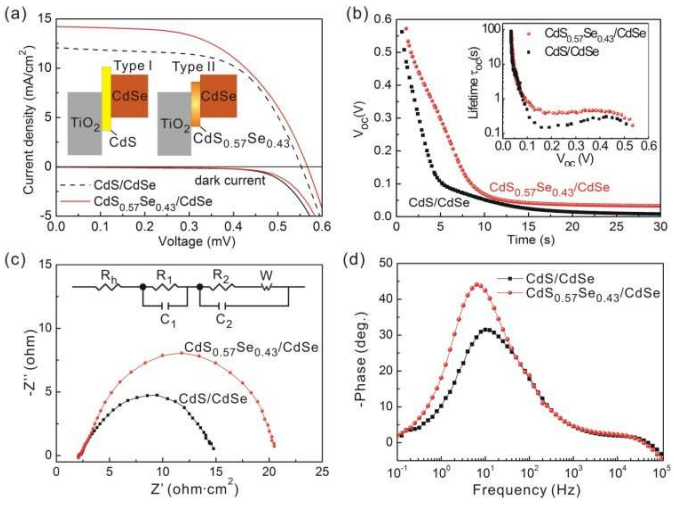

Fig. 7 (a) J–V characteristics of CdS/CdSe and $CdS_{0.57}Se_{0.43}$/CdSe QDSCs in the dark and under illumination (100 mW/cm^2), along with schematic interfacial band diagrams for CdS/CdSe (type I) and $CdS_{0.57}Se_{0.43}$/CdSe (type II). (b) Time-dependence of V_{oc} in CdS/CdSe and $CdS_{0.57}Se_{0.43}$/CdSe QDSCs, as determined by open-circuit voltage decay analysis. The inset is the V_{oc} decay of the corresponding cells as determined by open-circuit voltage decay analysis. (c) Electrochemical impedance spectra and (d) Bode plots of CdS/CdSe and $CdS_{0.57}Se_{0.43}$/CdSe QDSCs measured by applying an oscillation potential of 0.55 V from 10^5 to 10^{-1} Hz. The inset in (c) is a schematic diagram of the equivalent circuit used to model the experimental data.

IMVS was performed under a laser source (λ = 446 nm) at various light intensities to gauge the dynamics of charge recombination in the QDSCs. The logarithm of τ_{oc} was linearly related to V_{oc} (Fig. 6b). The results indicates that the carrier lifetime of a representative device sensitized with $CdS_{0.57}Se_{0.43}$/CdSe QDs (x = 0.43) was larger than that of a device sensitized with CdS/CdSe QDs. The J-V characteristics of QDSCs based on $CdS_{0.57}Se_{0.43}$/CdSe QDs and CdS/CdSe QDs both in the dark and under illumination (100 mW/cm^2) were extracted (Fig. 7a). A solar cell with $CdS_{0.57}Se_{0.43}$ QDs as the interlayer exhibited higher J_{sc}, V_{oc}, and η values than a cell sensitized with CdS/CdSe QDs. The $CdS_{0.57}Se_{0.43}$/CdSe QDSC achieved the following performance characteristics: J_{sc} = 14.22 mA/cm^2, V_{oc} = 566.8 mV, and η = 4.46%. The performance characteristics of the CdS/CdSe QDSC were as follows: J_{sc} =12.07 mA/cm^2, V_{oc} = 552.9 mV, and η = 4.09%. Whereas the J_{sc} and V_{oc} values were improved by replacement of the CdS QD with $CdS_{0.57}Se_{0.43}$ QDs, the opposite trend was observed for FF, which decreased from 61.3% to 55.3%.

The inset of Fig. 7a illustrates the proposed heterojunction structure at the TiO_2 nanoparticle surfaces. Because a type I junction existed at the CdS/CdSe interface, electron injection from the CBM of CdSe into the TiO_2 nanocrystals was impeded by the CdS nanocrystal layer, as has previously been reported.[37] Excited electrons located at the CdS/CdSe interface and surface traps from CdSe QDs had a large probability of recombining with the holes in electrolyte, resulting in decreased cell performance. In contrast, a $CdS_{0.57}Se_{0.43}$ QD layer with a relatively low CBM formed a type II staircase heterojunction, which resulted in increased electron injection yield from the CdSe QDs into TiO_2 and reduced charge recombination. The transition from a type I CdS/CdSe heterojunction to a type II staircase $CdS_{1-x}Se_x$/CdSe heterojunction depended on the diameter of the QDs, their Fermi levels, and the Se fraction in the $CdS_{1-x}Se_x$ QDs.

Two attractive notations should pay attention in the developed staircase TiO_2/$CdS_{0.57}Se_{0.43}$/CdSe photoanode. First, the optimized potential barrier of two interfaces: TiO_2/$CdS_{0.57}Se_{0.43}$ and $CdS_{0.57}Se_{0.43}$/CdSe are obviously different. Second, the CBM of CdSe QDs are raised after introducing of $CdS_{0.57}Se_{0.43}$ QDs as interlayer. It is known that the difference of CBM should over 0.2 eV for effective electrons injection from donors to TiO_2, as the driven force would be large enough to compete with the relaxation and recombination processes.[38] The potential barrier of TiO_2/$CdS_{0.57}Se_{0.43}$ (0.21 eV) is agree with the theoretical speculation. In contrast, the barrier difference between $CdS_{0.57}Se_{0.43}$ and CdSe can be reduced as low as 0.03 eV while the electrons injection is still promising. One explanation is that the electrons injection is dependent on the crystal lattice parameters of contact semiconductors.[39] The lattice mismatch between TiO_2 and Cd chalcogenide is large than 15%, while it is less than 4% for (001) planes between $CdS_{1-x}Se_x$ and CdSe.[24,40] The matched crystal structure between $CdS_{1-x}Se_x$ and CdSe will facilitate the effective charge injection. Another reason is attributed to the different exciton

binding energy of the semiconductors (TiO_2 ~60 meV,[41] CdS ~ 28 meV,[42] CdSe ~ 13 meV[43] in bulk materials). "In principle, the exciton binding energy in QDs is larger than bulk materials due to the quantum confinement effect, which is accounted in condition that an infinite barrier height exists.[44,45] As the barrier height between CdSe and interlayer $CdS_{1-x}Se_x$ is quite closed (e.g. 0.03 eV between $CdS_{0.57}Se_{0.43}$ and CdSe), their binding energy tends to similar as bulk nanocrystals." The lowest exciton binding energy of CdSe indicated their smallest Coulomb force to confine the excited electrons, resulting in their effective electrons injection across the $CdS_{1-x}Se_x$/CdSe interfaces.

Compared with bare CdSe QDs deposited on TiO_2, the conduction band of CdSe QDs is lifted up modestly by the interlayer $CdS_{1-x}Se_x$ QDs. This phenomenon can be easy explained by the situation of Fermi level alignment which is dependent on the conductivity of semiconductors.[46] Herein, we firstly show the quantificationally change of the potential difference in two interfaces, $TiO_2/CdS_{1-x}Se_x$ and $CdS_{1-x}Se_x$ /CdSe in co-sensitized QDSCs. The method of introducing the ternary QDs as interlayer can effectively tune the potential of both interfaces, which is a general way to facilitate the electrons injection and improve efficiency in all kind of co-sensitized QDSCs.

Next, we carried out open-circuit voltage decay analysis to evaluate the charge recombination process. Fig. 7b shows the variation of time dependent V_{oc} decay for cells with the decay starting at the moment of interruption of light power. The electron lifetime can be determined from the voltage decay with time according to

$$\tau_{oc} = -\frac{k_B T}{e}\left(\frac{dV_{oc}}{dt}\right)^{-1} \quad (2)$$

where τ_{oc} is the recombination lifetime, k_B is the Boltzmann constant (1.38×10^{-23} J/K), T is the absolute temperature (300 K), and e is the electronic charge (1.602×10^{-19} C).[32]

The correlation of lifetime with V_{oc} is plotted in the inset of Fig. 7b. At a given V_{oc}, the recombination lifetime of cells sensitized with $CdS_{0.57}Se_{0.43}$/CdSe was greater than that of cells sensitized with CdS/CdSe. The longer recombination lifetime of the former confirms that the ample coverage of the staircase $CdS_{0.57}Se_{0.43}$/CdSe heterostructure increased charge injection and resulted in low probability of back electron transfer. The reduced recombination lifetime in the $CdS_{0.57}Se_{0.43}$/CdSe QDSC compared to that in the CdS/CdSe QDSC led to the higher V_{oc} of the former.

We measured the electrochemical impedance spectra of the two kinds of QDSCs by applying a potential of 0.55 V by modeling with an equivalent circuit (Fig. 7c). The two semicircular curves, a small one at 1–100 kHz and a large one at 0.1–1 kHz, were ascribed to charge transfer resistance at the counter electrode/electrolyte interface (R_1) and the recombination resistance at the TiO_2/QDs/electrolyte interface (R_2), respectively.[47] The recombination resistance of a QDSC based on $CdS_{0.57}Se_{0.43}$/CdSe (18 ohm) was larger than that of a CdS/CdSe QDSC (12.5 ohm). The electron lifetime ($1/2\pi f_{max}$) can be derived from the Bode phase plots of the electrochemical impedance spectra (Fig. 7d), which display the frequency peaks of the charge transfer process at different interfaces for these two QDSCs. The electron lifetime was 25.2 ms for $CdS_{0.57}Se_{0.43}$/CdSe QDSCs and 15.9 ms for CdS/CdSe QDSCs. The longer lifetime for the former confirms that the type II staircase heterojunction at the TiO_2 nanoparticle surface effectively reduced back electron transfer.

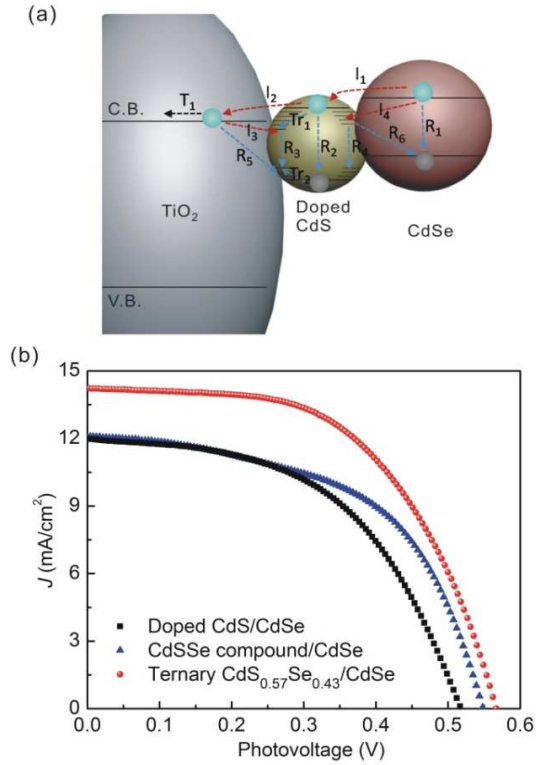

Fig. 8 (a) Charge injection and recombination processes for photogenerated electrons (green arrows) and holes (blue arrow) in photoanode in QDSCs. Each arrow could denote more than one process. Injection (red dashed arrow), trapping and recombination (blue dashed arrow), and transport (black dashed arrow) are indicated. (b) $J-V$ characteristics of solar cells sensitized with Zn-doped CdS/CdSe QDs, Se-doped CdS/CdSe QDs and $CdS_{0.57}Se_{0.43}$/CdSe QDs.

To demonstrate the charge injection and recombination processes of ternary $CdS_{0.57}Se_{0.43}$/CdSe and doped-CdS/CdSe QDSCs, a schematic for photogenerated electrons and holes in doped QDSCs photoanode are demonstrated in Fig. 8a. Excited electrons can be injected from the conduction band of CdSe QDs to CdS QDs (I_1) and wide band gap TiO_2 nanoparticles (I_2). Injected electrons in the conduction band of wide band gap semiconductor can be transported (T_1) to conductive FTO glass or back injected in the traps of CdS QDs (I_3). Processes I_1, I_2, and T_1 are required for solar cell operation which is necessarily to compete with recombination processes. For the doped CdS QDs with dopent introduced traps, electrons in conduction band of CdS QDs can be trapped (Tr_1) into its trap states, depending on the band alignment, while the holes are fast trapped in band gap states (Tr_2). Inside of the semiconductor, the direct recombination is induced by the photogenerated electron-hole pairs, R_1 and R_2, or through trap states, R_3 and R_4. On the other hand, electrons in the conduction band of the TiO_2 and CdS traps would recombine with trapped holes in the CdS QDs (R_5) and CdSe valence band (R_6).

Our surface ion transfer method of tailoring the bandgap of nanostructured semiconductors is to make an alloy of two semiconductors, CdS and CdSe, with different energy gaps. Composition dependent bandgap engineering arises from a dependence of a homogenously crystal lattice change, without introducing the dopants and traps states. The recombination of R_3-R_6 can be avoided in the alloyed system.

J−*V* characteristics of solar cells sensitized with Zn-doped CdS/CdSe QDs and Se-doped CdS/CdSe QDs and $CdS_{0.57}Se_{0.43}$/CdSe QDs are demonstrated in Fig. 8b. The interlayer $CdS_{0.57}Se_{0.43}$ QDs without traps resulted in lower recombination compared with the doped ones. Consequently, larger V_{oc} values were obtained for cells sensitized with $CdS_{0.57}Se_{0.43}$/CdSe QDs than for cells sensitized with Zn-doped CdS/CdSe QDs and Se-doped CdS/CdSe QDs (Fig. 8b). Cells sensitized with the $CdS_{0.57}Se_{0.43}$ /CdSe, Zn-doped CdS/CdSe QDs and Se-doped CdS/CdSe QDs exhibited V_{oc} values of 566.8, 517.7, and 548.5 mV. The performance characteristics obtained with the types of QDs are summarized in Table S2. The highest shunt resistance of $CdS_{0.57}Se_{0.43}$/CdSe QDSCs indicates its lowest leakage current, which further confirm the less traps in our ternary $CdS_{0.57}Se_{0.43}$ QDs than the doped CdS QDs. Besides, the low series resistance of ternary $CdS_{0.57}Se_{0.43}$/CdSe QDSCs contributes its relatively higher FF (0.55). This result indicates the designed ternary $CdS_{0.57}Se_{0.43}$/CdSe QDSCs not only enhance the charge injection, but also keep a fairly high FF as well as not introduce the traps states inside the QDs.

3. Conclusions

We introduced a series of annealed $CdS_{1-x}Se_x$ QDs as potential-tuning interlayer to realign the band structures of the CdSe based QDSCs. By controlling the Se content in the $CdS_{1-x}Se_x$ QDs, we tuned their conduction band minimum to generate suitable potential driving force at the interfaces on its both sides, TiO_2/$CdS_{1-x}Se_x$ and $CdS_{1-x}Se_x$/CdSe, which resulted in an optimized staircase band structure. The $CdS_{1-x}Se_x$ QDs interlayer reduced the lattace mismatch between TiO_2 and CdSe QDs as well. Compared with the TiO_2/CdS/CdSe heterojunction, the TiO_2/$CdS_{0.57}Se_{0.43}$/CdSe heterojunction with finely tuned type II staircase provided energetic driving force simultaneously adequate for both the exciton dissociation at the $CdS_{0.57}Se_{0.43}$/CdSe interface and the electron injection at the TiO_2/$CdS_{0.57}Se_{0.43}$ interface. It resulted in a ~15% improvement in electron injection efficiency with reduced charge recombination. A solar cell with $CdS_{0.57}Se_{0.43}$ QDs interlayer achieved an 17.8% enhancement in photocurrent density and the maximum power conversion efficiency as high as 4.46% under 1 sun illumination. It strongly suggested that using ternary QDs as potential tuning layer represent a promising method for efficient electron injection in QDSCs.

Acknowledgements

We acknowledge financial support from Core Research for Evolutional Science and Technology (CREST) of the Japan Science and Technology Agency. The authors thank Dr. Masatoshi Yanagida and Dr. Ashraful Islam from NIMS for valuable discussions.

Notes and references

[a]*Photovoltaic Materials Unit, National Institute for Materials Science (NIMS), Tsukuba, Ibaraki, 305-0047, Japan*
[b]*State Key Laboratory of Metal Matrix Composites, Shanghai Jiaotong University, Shanghai 200240, China*
** E-mail: Yang.Xudong@nims.go.jp(X. D. Yang); Han.Liyuan@nims.go.jp(L. Y. Han)*

Electronic Supplementary Information (ESI) available: [details of any supplementary information available should be included here]. See DOI: 10.1039/b000000x/

1 H. S. Kim, C. R. Lee, J. H. Im, K. B. Lee, T. Moehl, A. Marchioro, S. J. Moon, R. H. Baker, J. H. Yum, J. E. Moser, M. Grätzel, N. G. Park, *Sci. Rep.*, 2012, **2**, 591: 1–7.
2 L. Cademartiri, E. Montanari, G. Calestani, A. Migliori, A. Guagliardi, G. A. Ozin, *J. Am. Chem. Soc.* 2006, **128**, 10337–10346.
3 A. Kongkanand, K. Tvrdy, K. Takechi, M. Kuno, P. V. Kamat, *J. Am. Chem. Soc.*, 2008, **130**, 4007–4015.
4 R. T. Ross, A. J. Nozik, *J. Appl. Phys.*, 1982, **53**, 3813.
5 R. D. Schaller, V. I. Klimov, *Phys. Rev. Lett.*, 2004, **92**, 186601.
6 R. D. Schaller, V. M. Agranovich, V. C. Klimov, *Nat. Phys.*, 2005, **1**, 189.
7 K. Tvrdy, P. A. Frantsuzovc, P. V. Kamat, *PNAS*, 2011, **108**, 29–34.
8 J. Bisquert, A. Zaban, M. Greenshtein, I. M. Sero, *J. Am. Chem. Soc.*, 2004, **126**, 13550–13559.
9 H. J. Lee, J. Bang, J. Park, S. Kim, S. M. Park, *Chem. Mater.* 2010, **22**, 5636-5643.
10 C. Li, L. Yang, J. Xiao, Y. C. Wu, M. Sondergaard, Y. Luo, D. M. Li, Q. B. Meng, B. B. Iversen, *Phys. Chem. Chem. Phys.*, 2013, **15**, 8710–8715.
11 V. G. Pedroa, C. Simaabc, G. Marzaria, P. P. Boixa, S. Giménezа, Q. Shende, T. Dittrichf, and I. M. Seró, *Phys. Chem. Chem. Phys.*, 2013, **15**, 13835-13843.
12 H. M. Cheng, K. Y. Huang, K. M. Lee, P Yu, S. C. Lin, J. H. Huang, C. G. Wu, J. Tang, *Phys. Chem. Chem. Phys.* 2012, **14**, 13539-48.
13 C. F. Chi, H. W. Cho, H. S. Teng, C. Y. Chuang, Y. M. Chang, Y. J. Hsu, Y. L. Lee, *Appl. Phys. Lett.* 2011, **98**, 012101.
14 Y. L. Lee, Y. S. Lo, *Adv. Funct. Mater.*, 2009, **19**, 604–609.
15 J. Zhang, N. Tansu, *J. Appl. Phys.* 2011, **110**, 113110.
16 Z. Wang, N. Xiang, Q. Wang, G. Zhang, M. Gong, *Journal of Luminescence*, 2010, **130**, 35-37.
17 F. Qian, Y. Li, S. Gradecak, H. G. Park, Y. Dong, Y. Ding, Z. L. Wang, C.M. Lieber, *Nature Materials* 2008, **7**, 701.
18 Y. K. Liu, J. A. Zapien, Y. Y. Shen, C. Y. Geng, C. S. Lee, S. T. Lee, *Adv. Mater.* 2005, **17**, 1372–1377.
19 P. K. Santra, P. V Kamat, *J. Am. Chem. Soc.*, 2012, **134**, 2508–2511.
20 M. A. Hossain, J. R. Jennings, N. Mathews, Q. Wang, *Phys. Chem. Chem. Phys.*, 2012, **14**, 7154.
21 T. Shu, Z. M. Zhou, H. Wang, G. H. Liu, P. Xiang, Y. G. Rong, H. E. Han, Y. D. Zhao, *J. Mater. Chem.*, 2012, **22**, 10525.

22 S. Ito, T. N. Murakami, P. Comte, P. Liska, C. Grätzel, M. K. Nazeeruddin, M. Grätzel, *Thin Solid Films*, 2008, **516**, 4613–4619.
23 X. D. Yang, M. Yanagida, L. Y. Han, *Energy Environ. Sci.*, 2013, **6**, 54-66.
24 Z. H. Chen, W. Q. Peng, K. Zhang, J. Zhang, M. Yanagida, L. Y. Han, *Nanoscale*, 2012, **4**, 7690–7697.
25 J. Xu, C. S. Lee, Y. B. Tang, X. Chen, Z. H. Chen, W. J. Zhang, S. T. Lee, X. X. Zhang, Z. H. Yang, *ACS Nano*, 2010, **4**, 1845–1850.
26 V. G. Pedro, X. Q. Xu, I. M. Sero, J. Bisquert, *ACS Nano*, 2010, **4**, 5783–5790.
27 J. Tauc, R. Grigorovici, A. Vancu, *Phys. Status Solidi B*, 1966, **15**, 627–637.
28 M. Grätzel, *Nautre*, 2001, **414**, 338–344.
29 H. S. Kim, C. R. Lee, J. H. Im, K. B. Lee, T. Moehl, A. Marchioro, S. J. Moon, R. H. Baker, J. H. Yum, J. E. Moser, M. Grätzel, N. G. Park, *Scientific Reports*, 2012, **2**:591, 1–7.
30 Y. L. Lee, C. F. Chi, S. Y. Liau, *Chem. Mater.* 2010, **22**, 922–927.
31 K. H. Lin, C. Y. Chuang, Y. Y. Lee, F. C. Li, Y. M. Chang, *J. Phys. Chem. C*, 2012, **116**, 1550–1555.
32 T. Zewdu, J. N. Clifford, J. P. Hernandez, E. Palomares, *Energy Environ. Sci.*, 2011, **4**, 4633–4638.
33 D. A. Hossain, J. R. Jennings, C. Shen, J. H. Pan, Z. Y. Koh, N. Mathews, Q. Wang, *J. Mater. Chem.*, 2012, **22**, 16235–16242.
34 J. Tian, R. Gao, Q. Zhang, S. Zhang, Y. Li, J. Lan, X. Qu, G. Z. Cao, *J. Phys. Chem. C*, 2012, **116**, 18655–18662.
35 Y. Tachibana, K. Hara, K. Sayama, H. Arakawa, *Chem. Mater.*, 2002, **14**, 2527–2535.
36 J. Bisquert, A. Zaban, M. Greenshtein, I. M. Sero, *J. Am. Chem. Soc.*, 2004, **126**, 13550–13559.
37 S. Emin, M. Yanagida, W. Q. Peng, L. Y. Han, *Sol. Energy Mater. Sol. Cells*, 2012, **101**, 5-10.
38 R. Katoh, A. Furube, K. Hara, S. Murata, H. Sugihara, H. Arakawa, M. Tachiya, *J. Phys. Chem. B*, 2002, **106**, 12957.
39 T. Wosinski, O. Yastrubchak, A. Makosa, T. Figielski, *J. Phys.: Condens. Matter*, 2000, **12** 10153.
40 Y. Li, L. Wei, X. Chen, R. Zhang, X. Sui, X. Y. Chen, J. Jiao, L. Mei, *Nanoscale Research Letters* 2013, **8**, 67.
41 L. Lin, Y. Yang, L. Men, X. Wang, D. He, Y. Chai, B. Zhao, S. Ghoshroy, Q. Tang, *Nanoscale*, 2013, **5**, 588-593.
42 B. Liu, R. Chen, X. L. Xu, D. H. Li, Y. Y. Zhao, Z. X. Shen, Q. H. Xiong, H. D. Sun, *J. Phys. Chem. C* 2011, **115**, 12826–12830.
43 A. Joshi, K. Y. Narsingi, M. O. Manasreh, E. A. Davis, B. D. Weaver, *Appl. Phys. Lett.* 2006, **89**, 131907.
44 J. M. Elward, A. Chakraborty, *Phys. Rev. B*, 1992, **45**, 3410-3417.
45 L. E. Brus, *J. Chem. Phys.* 1984, **80**, 4403-4409.
46 X. F. Gao, W. T. Sun, G. Ai, L. M. Peng, *Appl. Phys. Lett.* 2010, **96**, 153104.
47 J. Y. Liao, H. P. Lin, H. Y. Chen, D. B. Kuang, C. Y. Su, *J. Mater. Chem.*, 2011, **22**, 1627–1633.

